

Extended phase-matching conditions for improved entanglement generation

Vittorio Giovannetti, Lorenzo Maccone, Jeffrey H. Shapiro, and Franco N. C. Wong
*Massachusetts Institute of Technology, Research Laboratory of Electronics,
Cambridge, Massachusetts 02139.*

(Dated: May 1, 2019)

Extended phase-matching conditions for spontaneous parametric down-conversion are examined. By augmenting the conventional phase-matching conditions, they permit the creation of a class of frequency-entangled states that generalizes the usual twin-beam biphoton state. An experimental characterization of these states is possible through interferometric coincidence counting.

PACS numbers: 42.50.Dv, 03.65.Ud, 03.67.-a, 42.25.Hz

I. INTRODUCTION

Entanglement is the cornerstone of quantum information technology. Its wide-ranging applications include tests of the foundations of quantum mechanics, implementations of quantum algorithms, cryptographic communication procedures, measurement-accuracy enhancements, *etc.* Arguably, the most important source of entanglement is spontaneous parametric down-conversion (SPDC) in nonlinear optical crystals. In the down-conversion process, a photon from an intense pump beam is absorbed in a nonlinear crystal and two different photons (conventionally called signal and idler) are created. Energy conservation dictates that the frequencies of the signal and idler photons sum to that of the pump photon. Frequency entanglement arises from quantum superposition of the various ways in which this energy constraint is fulfilled by signal and idler photons belonging to a certain frequency interval. This interval is governed by phase-matching within the nonlinear crystal, a condition which is dependent on the crystal's length and the refractive indices along its principal optical axes [1].

In this paper we show how to obtain new kinds of frequency-entanglement by generalizing the conventionally used phase-matching condition. The resulting biphoton states, which were previously obtained by Erdmann, Branning, Grice and Walmsley in [2], can be characterized using two interferometers based on the Hong-Ou-Mandel and on the Mach-Zehnder setups, as described below. As will be shown, the extended conditions can be fulfilled with available crystals. They allow the use of long nonlinear crystals that improve the generation efficiency. Furthermore, they allow the use of short-duration pump pulses that increase the experimental signal-idler generation rate compared to that of continuous-wave (cw) pumping. These two advantages are not readily available with the conventional phase-matching condition: on one hand the use of long type II phase-matched crystals narrows the spectrum over which the down-converted photons are entangled, and, on the other hand, the use of pulsed pumping reduces the entanglement because the indistinguishability of the down-converted photons is adversely affected [3, 4, 5].

The paper is organized as follows. In Sect. II we in-

roduce our notation and give a brief derivation of the conventional phase-matching condition. In Sect. III we derive the extended phase-matching conditions and analyze their role in obtaining frequency entanglement. The following Sect. IV shows how one can obtain polarization entanglement starting from the states found in Sect. III. In Sect. V two experimental setups that can be used to characterize the frequency entanglement are described and analyzed. Appendix A closes the paper with the detailed visibility derivation for the interference experiments discussed in Sect. V.

II. BIPHOTON STATE VIA PARAMETRIC DOWN-CONVERSION

In this paper we employ continuous Fock space formalism, in which the photon annihilation operator $a_j(\omega)$ that destroys a photon of frequency ω in the j th mode obeys the commutation relation

$$[a_j(\omega), a_k^\dagger(\omega')] = \delta(\omega - \omega') \delta_{jk}. \quad (1)$$

To first order in the nonlinear interaction coupling $\chi^{(2)}$, the state of the system at the output of a compensated down-conversion crystal is the biphoton state [1, 2]

$$|\Psi\rangle = \int \frac{d\omega_s}{2\pi} \int \frac{d\omega_i}{2\pi} A(\omega_s, \omega_i) a_s^\dagger(\omega_s) a_i^\dagger(\omega_i) |0\rangle, \quad (2)$$

where $a_s(\omega)$ and $a_i(\omega)$ are the annihilation operators for signal s and idler i modes, respectively, and $|0\rangle$ is the vacuum state. In Eq. (2) the biphoton spectral amplitude $A(\omega_s, \omega_i)$ determines the frequency spectrum of the biphoton state: integrating its squared modulus over the frequency of one of the two modes yields the fluorescence spectrum of the other. If we neglect inconsequential normalization constants and assume colinear plane-wave propagation, $A(\omega_s, \omega_i)$ can be written as (employing the notation from [6])

$$A(\omega_s, \omega_i) = \alpha(\omega_s, \omega_i) \Phi_L(\omega_s, \omega_i), \quad (3)$$

where

$$\alpha(\omega_s, \omega_i) \equiv \frac{\sqrt{\omega_s \omega_i}}{n_s(\omega_s) n_i(\omega_i)} \mathcal{E}_p(\omega_s + \omega_i), \quad (4)$$

$$\Phi_L(\omega_s, \omega_i) \equiv \frac{\sin(\Delta k(\omega_s, \omega_i)L/2)}{\Delta k(\omega_s, \omega_i)/2}. \quad (5)$$

The quantity $\alpha(\omega_s, \omega_i)$ depends on the refractive indices, n_s and n_i , of the signal and idler modes in the nonlinear crystal, and on the pump fluorescence spectrum, $|\mathcal{E}_p(\omega)|^2$, which is centered at ω_p and has a bandwidth Ω_p . The refractive indices, together with the term $\sqrt{\omega_s \omega_i}$, can in general be considered as constants over the effective spectrum, so that $\alpha(\omega_s, \omega_i)$ is approximated by a function of the sum of the signal and idler photon frequencies, $\omega_s + \omega_i$. On the other hand, the quantity $\Phi_L(\omega_s, \omega_i)$ is the phase-matching function, which depends on the nonlinear crystal length L and on the phase mismatch

$$\Delta k(\omega_s, \omega_i) \equiv k_p(\omega_s + \omega_i) - k_s(\omega_s) - k_i(\omega_i), \quad (6)$$

where $k_{p,s,i}(\omega) \equiv \omega n_{p,s,i}(\omega)/c$ denote the wave numbers of the pump, signal and idler photons, respectively. Notice that k_p , k_s and k_i are not all independent in the birefringent crystals that are typically used for SPDC where $k_s(\omega) = k_i(\omega)$ for type I phase-matching, and

$k_p(\omega) = k_s(\omega)$ (or $k_p(\omega) = k_i(\omega)$) for type II phase-matching.

For frequency entanglement generation, the SPDC crystal is usually operated at frequency degeneracy, in which the signal and idler spectra are centered around half the mean frequency of the pump ω_p [3, 4, 5]. This is enforced by imposing the conventional phase-matching condition that requires the crystal's refractive indices to satisfy

$$n_p(\omega_p) = \frac{n_s(\omega_p/2) + n_i(\omega_p/2)}{2}. \quad (7)$$

Employing Eq. (7) and approximating the function Δk of Eq. (6) with a first-order Taylor expansion in ω_s and ω_i around $\omega_p/2$, we obtain

$$\Delta k(\omega_s, \omega_i) = (\omega_s - \omega_p/2)\gamma_s + (\omega_i - \omega_p/2)\gamma_i, \quad (8)$$

where $\gamma_s \equiv k'_p(\omega_p) - k'_s(\omega_p/2)$ and $\gamma_i \equiv k'_p(\omega_p) - k'_i(\omega_p/2)$. With this result, the biphoton state $|\Psi\rangle$ of Eq. (2) can be written as

$$|\Psi_{pm}\rangle = \int \frac{d\tilde{\omega}_s}{2\pi} \int \frac{d\tilde{\omega}_i}{2\pi} \alpha(\tilde{\omega}_s + \tilde{\omega}_i + \omega_p) \frac{\sin[(\gamma_s \tilde{\omega}_s + \gamma_i \tilde{\omega}_i)L/2]}{(\gamma_s \tilde{\omega}_s + \gamma_i \tilde{\omega}_i)/2} |\omega_p/2 + \tilde{\omega}_s\rangle_s |\omega_p/2 + \tilde{\omega}_i\rangle_i, \quad (9)$$

where $\tilde{\omega}_s = \omega_s - \omega_p/2$ and $\tilde{\omega}_i = \omega_i - \omega_p/2$ represent the signal and idler detunings from degeneracy, and $|\omega\rangle \equiv a^\dagger(\omega)|0\rangle$.

If the crystal is pumped with monochromatic light $\Omega_p \rightarrow 0$, then $\alpha(\omega) \rightarrow \delta(\omega - \omega_p)$ and the state $|\Psi_{pm}\rangle$ becomes

$$|\text{TB}\rangle \equiv \int \frac{d\tilde{\omega}}{2\pi} \frac{\sin(2\pi\tilde{\omega}/\Omega_f)L}{2\pi\tilde{\omega}/\Omega_f} |\omega_p/2 + \tilde{\omega}\rangle_s |\omega_p/2 - \tilde{\omega}\rangle_i \quad (10)$$

where

$$\Omega_f = \frac{4\pi}{L|\gamma_s - \gamma_i|}, \quad (11)$$

and a normalization constant has been omitted. In this limit, the fluorescence spectra of the two photons are identical and have a bandwidth Ω_f . In the case of type I phase-matching (for which $\gamma_s = \gamma_i$) the derivation of Eq. (9) would require one to include second-order terms in the expansion (8), because the first-order terms cancel [2]. In the following, for sake of simplicity, we limit our analysis to type II crystals for which the linear approximation is sufficient. The biphoton twin-beam state $|\text{TB}\rangle$ is a maximally frequency-entangled state in the sense that a frequency measurement on one photon exactly determines the outcome of a frequency measurement on the other photon. In particular, the frequencies of the signal and idler are anti-correlated: their sum is fixed and equal to the pump frequency.

Two experimental problems, connected with a finite pump bandwidth Ω_p and a finite crystal length L , arise when the conventional phase-matching condition is used to generate entanglement. If the pump spectrum is not perfectly monochromatic ($\Omega_p > 0$), a range of signal-idler sum frequencies exist such that the maximal entanglement property is degraded and the spectra of the two down-converted photons are no longer identical [4]. The drawback of non-identical signal and idler spectra turns out to be critical for many experiments that employ a pulsed pump, because the difference in the spectra introduces distinguishability that is detrimental to quantum interference [3, 4, 5, 7]. On the other hand, it is clear from Eq. (11) that the use of long crystals reduces the available bandwidth over which frequency entanglement occurs. In the limit of a long crystal no entanglement survives because signal and idler are both monochromatic photons of frequency $\omega_p/2$. However, from the experimental point of view, a long crystal is preferable because it increases down-conversion efficiency. Various experimental techniques aimed at preserving or recovering entanglement in the pulsed-pump regime have been studied [8]. In this paper, we approach these problems by extending the conventional phase-matching condition (7) in such a way that the signal and idler spectra remain indistinguishable for any pump bandwidth.

III. EXTENDED PHASE-MATCHING CONDITIONS

Under the conventional phase-matching condition for frequency-degenerate SPDC, and in the linear dispersion regime of Eq. (8), we have shown that the phase-matching function Φ_L is characterized by the two parameters γ_s and γ_i . Better physical insight may be gained by treating γ_s and γ_i as Cartesian coordinates and then converting to the polar-coordinates representation $\gamma_s = \gamma \cos \theta$ and $\gamma_i = \gamma \sin \theta$. The parameter θ controls the structure of the biphoton spectrum by governing the orientation of the symmetry axis $\tilde{\omega}_i = -\tilde{\omega}_s \tan \theta$ of the phase-matching function $\Phi_L(\omega_s, \omega_i)$. The parameter γ , on the other hand, controls the width of Φ_L and hence determines the bandwidth of the biphoton state. As will be shown, it is the parameter θ that effectively controls the “quality” of the frequency entanglement of the down-converted photons, thus determining their frequency correlations.

To enforce the indistinguishability of the down-converted signal and idler spectra, it is necessary to symmetrize the biphoton spectral amplitude $A(\omega_s, \omega_i)$ with

respect to ω_s and ω_i [4]. Given that $\alpha(\omega_s, \omega_i)$ of Eq. (4) can be approximated by a function of $\omega_s + \omega_i$, Eq. (3) suggests that we need only to symmetrize the phase-matching function $\Phi_L(\omega_s, \omega_i)$ to guarantee that $A(\omega_s, \omega_i)$ is symmetric in ω_s and ω_i . The simplest and best known way to achieve such symmetry is to require type I phase-matched crystals for which $k_s(\omega) = k_i(\omega)$. Interestingly, a whole new class of states is obtained by adopting a different strategy: the symmetrization of Φ_L can also be achieved by requiring $\gamma_s = -\gamma_i$ (i.e. $\theta = -\pi/4$). This regime can be enforced if the crystal, in addition to satisfying the conventional phase-matching condition (7), also satisfies the group velocity condition [2, 3, 6]

$$k'_p(\omega_p) = \frac{k'_s(\omega_p/2) + k'_i(\omega_p/2)}{2}. \quad (12)$$

Equations (7) and (12) force the system to be phase-matched over the entire fluorescence spectrum, not just at degeneracy. Together they constitute the extended phase-matching conditions that will be used in the rest of this paper [14]. Under these constraints, the state $|\Psi\rangle$ now becomes

$$|\Psi_{epm}\rangle = \int \frac{d\tilde{\omega}_s}{2\pi} \int \frac{d\tilde{\omega}_i}{2\pi} \alpha(\tilde{\omega}_s + \tilde{\omega}_i + \omega_p) \frac{\sin[\pi(\tilde{\omega}_s - \tilde{\omega}_i)/\Omega_f] L}{\pi(\tilde{\omega}_s - \tilde{\omega}_i)/\Omega_f} |\omega_p/2 + \tilde{\omega}_s\rangle_s |\omega_p/2 + \tilde{\omega}_i\rangle_i. \quad (13)$$

The biphoton spectral amplitude of this state is of the form

$$A(\omega_s, \omega_i) = S(\omega_s + \omega_i) D(\omega_s - \omega_i), \quad (14)$$

where $S \equiv \alpha$ is a function of the frequency sum $\omega_s + \omega_i$, and $D \equiv \Phi_L$ is a function of the frequency difference $\omega_s - \omega_i$. The symmetry properties of the extended-phase-matched $A(\omega_s, \omega_i)$ are such that, independent of the pump bandwidth Ω_p , the symmetry axis of the pump spectral function $\alpha(\omega_s + \omega_i)$ (with $\theta = \pi/4$) is orthogonal to the symmetry axis of the phase-matching function $\Phi_L(\omega_s - \omega_i)$ (with $\theta = -\pi/4$). In contrast, the symmetry axis of $\Phi_L(\omega_s, \omega_i)$ for a conventionally phase-matched state $|\Psi_{pm}\rangle$ is not specified and can take on any value of θ (see Fig. 1).

In the limit of a monochromatic pump, $\Omega_p \rightarrow 0$, we again obtain the twin-beam state $|\text{TB}\rangle$ from $|\Psi_{epm}\rangle$, suggesting that the additional phase-matching constraint Eq. (12) does not play a role in cw-pumped SPDC. On the other hand, even for pulsed pump, we may still obtain a maximally frequency-entangled state from $|\Psi_{epm}\rangle$ in the limit of infinite crystal length $L \rightarrow \infty$ [2, 6]. In this case one obtains the “difference-beam” state in which the signal and idler frequencies are equal, i.e.

$$|\text{DB}\rangle \equiv \int \frac{d\tilde{\omega}}{2\pi} \alpha(2\tilde{\omega} + \omega_p) |\omega_p/2 + \tilde{\omega}\rangle_s |\omega_p/2 + \tilde{\omega}\rangle_i, \quad (15)$$

where the spectral function of the state is now determined entirely by the pump spectral characteristics. As shown pictorially in Fig. 2, the properties of this $|\text{DB}\rangle$ state are complementary, via Fourier duality, to those of the $|\text{TB}\rangle$ state. A detailed comparison between the states $|\text{TB}\rangle$ and $|\text{DB}\rangle$ can be found in [6]. In this paper we will focus on the properties of the class of states $|\Psi_{epm}\rangle$ of Eq. (13) to which both $|\text{TB}\rangle$ and $|\text{DB}\rangle$ belong.

The states $|\Psi_{epm}\rangle$ comprise a family of frequency-entangled states each of which can be uniquely identified by the value of the two bandwidth parameters Ω_f of Eq. (11) and Ω_p . The parameter Ω_f derives from the phase-matching function Φ_L and is determined by the crystal properties alone. It sets the bandwidth of the frequency-difference part of the biphoton state. On the other hand, the parameter Ω_p , comes solely from the pump spectral function α and determines the bandwidth of the frequency-sum part of the biphoton state. The ideal cases of $|\text{TB}\rangle$ and $|\text{DB}\rangle$ are the maximally entangled extrema of this family of states. For finite L and nonzero Ω_p , the state $|\Psi_{epm}\rangle$ retains frequency entanglement even though it is no longer maximally entangled. Hence, a measurement of the frequency of one photon partially determines the frequency of the other. Nevertheless, the spectra of the two photons are the same and the state maintains optimal visibility in quantum inter-

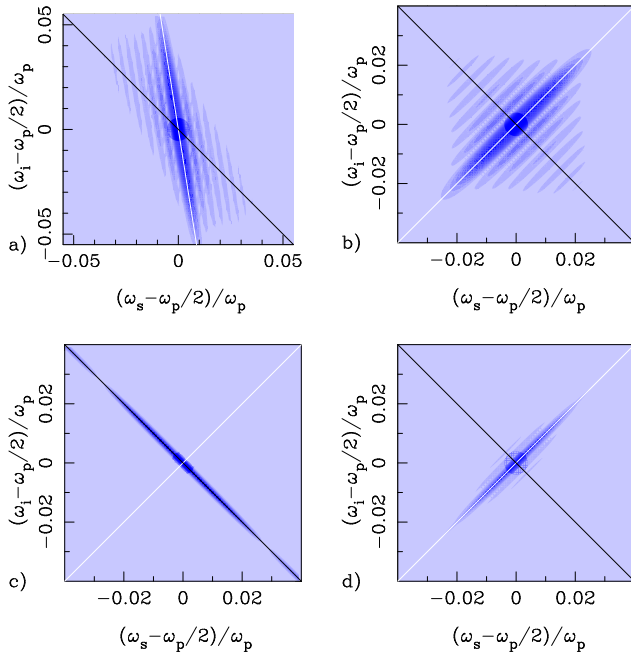


FIG. 1: Plots of the biphoton spectral amplitude $|A(\omega_s, \omega_i)|$ for different values of the crystal length L and pump bandwidth Ω_p . In each plot the white line is the symmetry axis of $\Phi_L(\omega_s, \omega_i)$ and the black line is the symmetry axis of $\alpha(\omega_s + \omega_i)$, which is chosen according to (27). **a)** Conventional phase-matching condition (7): the two symmetry axes are in general neither orthogonal nor coincident. (the parameters for this plot are $\theta = \pi/20$; $L = 1$ cm; $\Omega_p = 4 \times 10^{13} \text{ s}^{-1}$.) **b)** Extended phase-matching conditions (7) and (12): the two symmetry axes are orthogonal. ($\theta = -\pi/4$; $L = 1$ cm; $\Omega_p = 4 \times 10^{13} \text{ s}^{-1}$.) **c)** |TB>-like state (10): signal and idler photon frequencies are strongly anti-correlated. The |TB> state is reached by using either the conventional phase-matching condition or the extended ones in the limit of small bandwidth Ω_p . ($L = 0.1$ cm; $\Omega_p = 1.6 \times 10^{12} \text{ s}^{-1}$.) **d)** |DB>-like state (15): signal and idler frequencies are strongly positive-correlated. The |DB> state can *only* be obtained under the extended phase-matching conditions in the limit of very long crystals. ($L = 5$ cm; $\Omega_p = 4 \times 10^{13} \text{ s}^{-1}$.) For all the plots $\omega_p = 2 \times 10^{15} \text{ s}^{-1}$ and $\gamma = 8 \times 10^{-5} \text{ ps}/\mu\text{m}$.

ference experiments for all values of the pump bandwidth Ω_p . This aspect will be thoroughly analyzed in Sect. V, where some interferometric measurements to characterize these states are described.

The extended phase-matching conditions (7) and (12) have been obtained from the first-order Taylor-series expansion given in Eq. (8). This approximation for the function Φ_L of Eq. (5) is valid if the second-order correction to $\Delta k(\omega_s, \omega_i)$ introduces a contribution δ_k such that $\delta_k L/2$ is much smaller than $\pi/2$. In vector notation, this second-order term is given by $\frac{1}{2}(\vec{\omega} - \vec{\omega}_0) \cdot H(\vec{\omega}_0) \cdot (\vec{\omega} - \vec{\omega}_0)$ where $\vec{\omega} = (\omega_s, \omega_i)$, $\vec{\omega}_0 = (\omega_p/2, \omega_p/2)$, and $H(\vec{\omega}_0)$ is the Hessian matrix of the function $\Delta k(\vec{\omega})$ evaluated at $\vec{\omega}_0$. The second-order contribution can be shown to be smaller than $|\mu|\Omega_p^2/2$, where μ is the maximum-

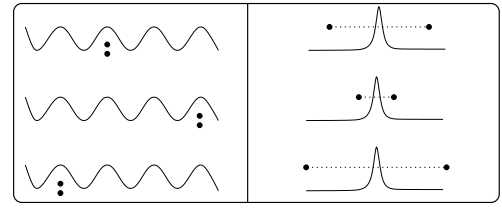


FIG. 2: Pictorial representation of the time domain description of parametric down-conversion. In the crystal, the signal and idler photons are created simultaneously within a coherence time of the pump. **Left box:** In the |TB> state generation, a cw pump (represented by the sine wave in the figure) is used and its (ideally infinite) coherence time is much longer than the average time that the generated photons need to traverse the crystal ($\sim L/c$). The two photons in the |TB> state are *time correlated* and, by Fourier duality, *frequency anti-correlated*. **Right box:** In the |DB> state generation, a narrow pump pulse and a long (ideally infinite) nonlinear crystal are required. In this case, the different dispersion that the two photons see while crossing the long nonlinear crystal after their generation tends to separate them. At the output of the crystal their separation depends on the position at which they were created. The extended phase-matching conditions, however, guarantee that the mean “position” of the two photons coincides with that of the pump pulse. Hence, the two photons in the |DB> state are *time anti-correlated* and *frequency correlated*.

magnitude eigenvalue of $H(\vec{\omega}_0)$. Hence, to ensure the validity of the first-order expansion in (8) over the entire pump spectrum Ω_p , we must require that $L \ll 8\pi/(|\mu|\Omega_p^2)$. An example of a nonlinear crystal that satisfies this requirements for type II extended phase-matching has been given in [6].

When the second-order contribution cannot be neglected, we can still obtain a biphoton spectral function of the form (14). This can be achieved by augmenting (7) and (12) with the requirement that

$$k_s''(\omega_p/2) = k_i''(\omega_p/2) = 2k_p''(\omega_p). \quad (16)$$

If contributions of order greater than or equal to three are non-negligible, then there is no way to impose the form of Eq. (14) to the spectral function $A(\omega_s, \omega_i)$. It is still possible, however, to force the maximum of the phase-matching function $\Phi_L(\omega_s, \omega_i)$ to lie in the region $\omega_s = \omega_i$, as in the case of the |DB> state. This is obtained by requiring that the n th order terms obey

$$\frac{\partial^n k_p}{\partial \omega^n}(\omega_p) = \frac{1}{2^n} \left[\frac{\partial^n k_s}{\partial \omega^n}(\omega_p/2) + \frac{\partial^n k_i}{\partial \omega^n}(\omega_p/2) \right]. \quad (17)$$

In the rest of the paper we will focus on cases in which the first-order approximation holds.

IV. POLARIZATION ENTANGLEMENT

Because the two photons of $|\Psi_{epm}\rangle$ are indistinguishable in frequency, it would be very useful to entangle them in polarization. A number of configurations can be utilized to achieve this goal. For example one can adopt a method analogous to the one presented in [9], in which the outputs from two coherently-pumped optical parametric amplifiers (OPAs) are entangled with a polarizing beam splitter. Here, we discuss a different scheme, based on the one presented in [10], that employs a single crystal. It generates the desired polarization-entangled state only 50% of the time, but a simple post-selection measurement allows one to discard the cases in which the polarization-entangled biphoton state is not present.

In a type II phase-matched crystal the down-converted photons have orthogonal polarizations, say \uparrow for the signal and \leftrightarrow for the idler. If these photons are fed into one port of a 50-50 beam splitter, then each of the two photons (which are distinguishable in polarization) has an equal chance of being transmitted or reflected. The state after the beam splitter is given by

$$|\Psi_{out}\rangle = \frac{1}{2} \int \frac{d\omega_s}{2\pi} \int \frac{d\omega_i}{2\pi} A(\omega_s, \omega_i) [c_{\uparrow}^{\dagger}(\omega_s) b_{\leftrightarrow}^{\dagger}(\omega_i) + b_{\uparrow}^{\dagger}(\omega_s) c_{\leftrightarrow}^{\dagger}(\omega_i) + b_{\uparrow}^{\dagger}(\omega_s) b_{\leftrightarrow}^{\dagger}(\omega_i) + c_{\uparrow}^{\dagger}(\omega_s) c_{\leftrightarrow}^{\dagger}(\omega_i)] |0\rangle, \quad (18)$$

where b and c are the output modes of the beam splitter. At the two output ports of the beam splitter, detectors with measurement intervals longer than the largest signal-idler time separation are used to measure the desired coincidences even though the two photons will not in general arrive exactly at the same time [6]. This post-selection scheme discards the cases in which both photons of a pair exit from the same beam-splitter output port, i.e., the last two terms of Eq. (18). The post-selected, filtered output is the Bell state

$$|\Psi^{(+)}\rangle = \frac{1}{\sqrt{2}} [|\uparrow\rangle|\leftrightarrow\rangle + |\leftrightarrow\rangle|\uparrow\rangle]. \quad (19)$$

The other three Bell states can be similarly obtained by appropriate addition of a polarization rotator and/or a π -rad phase shifter acting on one of the polarizations in one of the beam splitter output arms.

V. EXPERIMENTAL ENTANGLEMENT CHARACTERIZATION

In this section we show how the frequency entanglement of the family of states $|\Psi_{epm}\rangle$ can be characterized experimentally. The setups we describe are sketched in Fig. 3 and are based on the Hong-Ou-Mandel (HOM) interferometer [11] and on the Mach-Zehnder (MZ) interferometer [12]. The photodetectors 1 and 2 at the output of the interferometers measure the photo-coincidence rate $P(\tau)$ over a long-time (i.e., longer than the time duration

of the biphoton) detection window. The rate P is monitored for different values of the time delay τ between the two arms of the interferometers that can be varied by moving the 50-50 output beam splitter (BS). From the Mandel formula for photodetection [1], we find

$$P \propto \int_T dt_1 \int_T dt_2 \langle \Psi_{in} | E_1^{(-)}(t_1) E_2^{(-)}(t_2) \times E_2^{(+)}(t_2) E_1^{(+)}(t_1) | \Psi_{in} \rangle, \quad (20)$$

where $|\Psi_{in}\rangle$ is the state of the field at the interferometer input, T is the measurement interval of the detectors and $E_j^{(\pm)}$ refers to the negative and positive components of the electric field at the j th detector. When $|\Psi_{in}\rangle$ is a biphoton state such as Eq. (2), the expression (20) in the limit of long detection window $T \rightarrow \infty$ becomes

$$P \propto \int \frac{d\omega_1}{2\pi} \int \frac{d\omega_2}{2\pi} |\langle 0 | a_1(\omega_1) a_2(\omega_2) | \Psi_{in} \rangle|^2, \quad (21)$$

where a_1 and a_2 are the photon annihilation operators at the two detectors. In terms of the annihilation operators of the signal and idler, these are given by

$$a_1(\omega) = [a_s(\omega) e^{i\omega\tau} + a_i(\omega)] / \sqrt{2} \quad (22)$$

$$a_2(\omega) = [a_s(\omega) - a_i(\omega) e^{-i\omega\tau}] / \sqrt{2}$$

for the HOM interferometer setup and by

$$a_1(\omega) = [a_s(\omega)(e^{i\omega\tau} + 1) + a_i(\omega)(e^{i\omega\tau} - 1)] / 2 \quad (23)$$

$$a_2(\omega) = [a_s(\omega)(1 - e^{-i\omega\tau}) + a_i(\omega)(1 + e^{-i\omega\tau})] / 2$$

for the MZ interferometer setup.

If the biphoton spectral amplitude $A(\omega_s, \omega_i)$ is symmetric in its arguments, as in the case of $|\Psi_{epm}\rangle$, Eq. (21) becomes

$$P_{\pm}(\tau) \propto \int \frac{d\omega_1}{2\pi} \int \frac{d\omega_2}{2\pi} |A(\omega_1, \omega_2)|^2 \times (1 \pm \cos[(\omega_1 \pm \omega_2)\tau]), \quad (24)$$

where the minus signs apply to the HOM interferometer, and the plus signs apply to the MZ interferometer. Using Eq. (14), one can show that the two interferometers are sensitive to different parts of the biphoton spectrum:

$$P_{-}(\tau) \propto \int \frac{d\omega}{2\pi} |D(\omega)|^2 [1 - \cos(\omega\tau)], \quad (25)$$

$$P_{+}(\tau) \propto \int \frac{d\omega}{2\pi} |S(\omega)|^2 [1 + \cos(\omega\tau)], \quad (26)$$

i.e., the HOM measures the difference-frequency part of the biphoton spectrum of the state $|\Psi_{epm}\rangle$, and the MZ measures the sum-frequency part.

Consider first the HOM interferometer. Equation (25) yields the usual triangular Mandel dip for type II phase-matching (shown in Fig. 4) centered at $\tau = 0$ with a (base-to-base) width of $4\pi/\Omega_f$, which is determined by

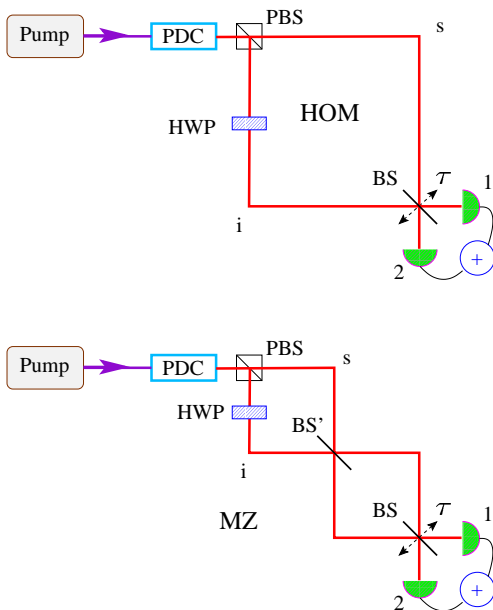


FIG. 3: Schematics of proposed experiments. The upper setup implements a Hong-Ou-Mandel interferometer that (under the extended phase-matching conditions) is sensitive to frequency anti-correlation of the down-converted photons. The lower setup is a Mach-Zehnder interferometer that is sensitive to positive frequency correlation. In both experiments the coincidences at detectors 1 and 2 are measured for different values of the relative delay τ between the two interferometer arms. The pump source produces a coherent pulse of mean frequency ω_p and bandwidth Ω_p that can be varied to create different types of entanglement. The configurations shown refer to type II phase-matched parametric down-converter (PDC) crystals for which a polarizing beam splitter (PBS) separates the signal and idler photons and the half wave plate (HWP) guarantees that the polarizations in the two output beams are the same.

the crystal length L . Note that the pump bandwidth Ω_p does not play any role in determining the function $P_-(\tau)$, which is a unique characteristic of the state $|\Psi_{epm}\rangle$ because of the extended phase-matching conditions. It is well known [3, 4, 5] that, under the conventional phase-matching condition (7) only, the visibility of the Mandel dip decreases when the pump bandwidth is increased. The Mandel dip can be interpreted as the result of destructive quantum interference between the different paths that lead to coincidences at the detectors [13]. If we are limited to the conventional phase-matching condition in type II phase-matched crystals, the two down-converted photons are distinguishable (for $\Omega_p > 0$) because their spectra are different [4]. In contrast, the extended phase-matching conditions ensure that the two spectra are equal (independent of Ω_p), thus maintaining indistinguishability of the two photons for all values of Ω_p . In this case, the visibility is not lost when the pump bandwidth Ω_p is increased [2]. This is evident from Fig. 5, where the visibilities of experiments employ-

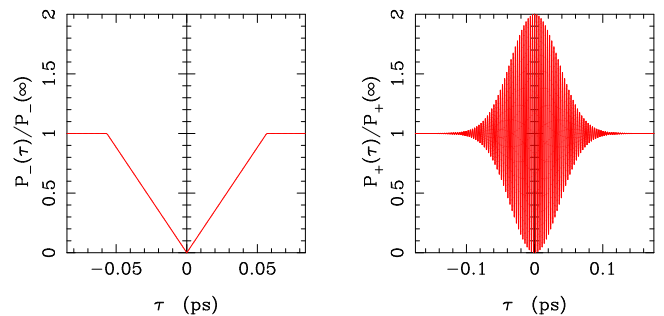


FIG. 4: Example of quantum signatures of the experimental results for a $|\Psi_{epm}\rangle$ input state. **Left:** Mandel dip in the coincidence rate $P_-(\tau)$ at the output of a HOM interferometer. The characteristic triangular shape of width $\propto 1/\Omega_f$ comes from the $\sin x/x$ form of the biphoton spectrum in (13). **Right:** Fringes and fringe envelope in the coincidence rate $P_+(\tau)$ at the output of the MZ interferometer. The Gaussian envelope of width $\propto 1/\Omega_p$ derives from the Gaussian spectral profile (27) of the pump beam. The parameters in the plots are $\gamma L = 8 \times 10^{-2}$ ps, $\omega_p = 2 \times 10^{15}$ s $^{-1}$ and $\Omega_p = 4 \times 10^{13}$ s $^{-1}$.

ing different phase-matching conditions are compared. A detailed analysis of the visibility is presented in App. A.

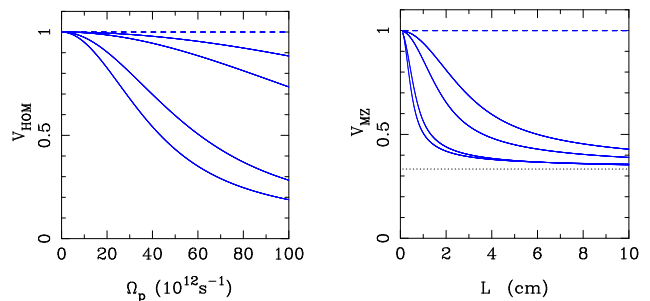


FIG. 5: **Left:** Plot of the Mandel-dip visibility V_{HOM} of Eq. (A4), which measures the dip depth in the HOM interferometer as a function of the pump bandwidth Ω_p . Here $\gamma = 8 \times 10^{-5}$ ps/ μm ; $L = 0.1$ cm. **Right:** Plot of the MZ-peak visibility V_{MZ} of Eq. (A8), which measures the amplitude of the modulation of the fringes of Fig. 4 as a function of the crystal length L . As discussed in appendix A, the MZ visibility is always greater than 33% (dotted line). Here $\gamma = 8 \times 10^{-5}$ ps/ μm ; $\Omega_p = 4 \times 10^{13}$ s $^{-1}$. For both plots different curves refer to different phase-matching conditions: extended phase-matching condition $\theta = -\pi/4$ (upper dashed line); conventional phase-matching condition (lower solid lines for, from top to bottom, $\theta = -\pi/5$, $\theta = -\pi/6$, $\theta = 0$, $\theta = \pi/5$). In both the HOM and MZ cases, under the conventional phase-matching condition the visibility decreases for increasing pump bandwidth [3, 4, 5] or crystal length. In contrast, there is no loss of visibility when the extended phase-matching conditions ($\theta = -\pi/4$) are employed.

Consider now the MZ interferometer. Equation (26) gives a peak centered at $\tau = 0$ with a width that is proportional to $1/\Omega_p$ and is determined by the pump spec-

trum. This peak is modulated by fringes of frequency ω_p and is totally independent of the crystal properties. An example is given in Fig. 4. For Gaussian pump spectrum

$$|\alpha(\omega)|^2 \propto \exp[-(\omega - \omega_p)^2/\Omega_p^2], \quad (27)$$

the coincidence function becomes

$$P_+(\tau) \propto 1 + \exp(-\Omega_p^2\tau^2/4) \cos(\omega_p\tau). \quad (28)$$

Similar fringes in coincidence counts have been experimentally observed under the conventional phase-matching condition in [12]. Analogous to the case of the HOM interferometer, if one drops the extended phase-matching conditions in favor of the conventional phase-matching condition (7), the visibility of the MZ peak decreases when L is increased. This effect is derived in App. A and illustrated in Fig. 5. Similar to the HOM dip, it is possible to interpret the loss of visibility in terms of loss of indistinguishability of the two down-converted photons.

As shown in Sect. III, each element of the family of states can be uniquely determined once the phase-matching bandwidth Ω_f of Eq. (11) and the pump bandwidth Ω_p are specified. It follows from the above analysis that the HOM interferometer cannot distinguish among $|\Psi_{epm}\rangle$ states with a fixed Ω_f but different Ω_p . It can only be used to discriminate among states with different Ω_f . On the other hand, the MZ interferometer cannot distinguish among states with a fixed Ω_p but different Ω_f . It can only discriminate among states with different pump bandwidths Ω_p . In order to obtain a complete characterization of the family of states $|\Psi_{epm}\rangle$, one needs to perform both HOM and MZ interferometric experiments. However, if one limits the analysis to the extremal cases of the states $|TB\rangle$ and $|DB\rangle$, either one of the two experiments is sufficient to distinguish between the two states because they are generated with different pump bandwidths *and* different crystal lengths.

Before concluding, some final remarks are in order. The unique characteristics of the $|\Psi_{epm}\rangle$ states originate from the symmetry properties imposed by the extended phase-matching conditions. These conditions allow the quantum correlations of the state to be more resilient. However, even for the conventionally phase-matched state $|\Psi_{pm}\rangle$ analogous properties could be obtained, if one were able to devise appropriate interferometric setups that somehow compensate for the difference between the signal and idler spectra (e.g., by stretching the bandwidth of one of them). In this respect we can say that the fundamental difference between the $|\Psi_{epm}\rangle$ and $|\Psi_{pm}\rangle$ states is in the fact that the former requires simpler and more easily realizable setups for demonstrating nonclassical features of the quantum states.

VI. CONCLUSIONS

We have discussed spontaneous parametric down-conversion in the regimes of continuous-wave pumping

and pulsed pumping. By adding to the conventional crystal phase-matching condition (7) the constraint (12), it is possible to enforce certain symmetry properties on the biphoton spectral function $A(\omega_s, \omega_i)$. This allows one to create a down-converted pair of photons with identical spectra that, under accessible experimental conditions, constitutes a maximally-entangled biphoton whose component photons have coincident frequencies. We have proposed and analyzed two experimental arrangements, based on the HOM and MZ interferometers, that can be used to characterize the states that exit an extended-phase-matched crystal. In particular, we have shown that extended-phase-matched states retain maximal visibility on both the interferometers for all the pump spectra. As in the case of the conventional phase-matching, it is possible to create polarization entanglement by exploiting the frequency entanglement: we have described a post-selective entangling procedure.

APPENDIX A: VISIBILITY OF HOM AND MZ INTERFEROMETERS

In this appendix we derive the expressions for the visibility functions V_{HOM} and V_{MZ} of the two experiments that were discussed in Sect. V.

We have already analyzed extended-phase-matched crystals. In the case of conventionally phase-matched crystals, where Eq. (12) does not hold, the expressions for the photo-coincidence rates $P_{\pm}(\tau)$ of Eqs. (25) and (26) are no longer valid. However, starting from Eq. (21), one can obtain the rate for the Hong-Ou-Mandel interferometer as

$$P_-(\tau) \propto \int \frac{d\tilde{\omega}_1}{2\pi} \int \frac{d\tilde{\omega}_2}{2\pi} |\alpha(\tilde{\omega}_1 + \tilde{\omega}_2 + \omega_p)|^2 \quad (A1)$$

$$\left| \phi_L(\gamma_s\tilde{\omega}_2 + \gamma_i\tilde{\omega}_1) - \phi_L(\gamma_s\tilde{\omega}_1 + \gamma_i\tilde{\omega}_2) e^{i(\tilde{\omega}_1 - \tilde{\omega}_2)\tau} \right|^2,$$

where $\phi_L(x) = 2 \sin(xL/2)/x$. For a Gaussian pump spectrum $|\alpha(\omega)|^2$ of the form (27), Eq. (A1) reduces to

$$P_-(\tau) \propto \begin{cases} 1 - \frac{\sqrt{\pi}}{2}\xi \operatorname{Erf}\left(\frac{1 - |\tau|/\tau_\theta}{\xi}\right) & \text{for } |\tau| < \tau_\theta \\ 1 & \text{for } |\tau| > \tau_\theta, \end{cases} \quad (A2)$$

where $\operatorname{Erf}(x) = \frac{2}{\sqrt{\pi}} \int_0^x dy e^{-y^2}$ is the error function and

$$\xi \equiv 4/\left(\Omega_p\gamma L|\cos\theta + \sin\theta|\right)$$

$$\tau_\theta \equiv \gamma L|\cos\theta - \sin\theta|/2. \quad (A3)$$

For $\xi \rightarrow \infty$, $P_-(\tau)$ reduces to the familiar triangular-shaped Mandel dip plotted in Fig. 4. This limit can be achieved for vanishing pump bandwidth $\Omega_p \rightarrow 0$, i.e. when a $|TB\rangle$ state is fed into the interferometer. Another way to obtain the same limit is to employ the extended phase-matching conditions ($\theta = -\pi/4$). This implies that an extended-phase-matched crystal will always

show perfect visibility for any value of the pump bandwidth Ω_p . The visibility is defined as the depth of the dip of Eq. (A2), i.e.

$$V_{HOM} \equiv \frac{P_-(\infty) - P_-(0)}{P_-(\infty) + P_-(0)} = \frac{\frac{\sqrt{\pi}}{2}\xi \operatorname{Erf}(1/\xi)}{2 - \frac{\sqrt{\pi}}{2}\xi \operatorname{Erf}(1/\xi)}. \quad (\text{A4})$$

It is plotted as a function of Ω_p for different values of θ in Fig. 5.

The case of the Mach-Zehnder interferometer is analogous, but now Eq. (21) becomes

$$P_+(\tau) \propto \int \frac{d\tilde{\omega}_1}{2\pi} \int \frac{d\tilde{\omega}_2}{2\pi} |\alpha(\tilde{\omega}_1 + \tilde{\omega}_2 + \omega_p)|^2 \times \left| \phi_L(\gamma_s \tilde{\omega}_2 + \gamma_i \tilde{\omega}_1) \sin \left[\left(\tilde{\omega}_1 + \frac{\omega_p}{2} \right) \frac{\tau}{2} \right] \sin \left[\left(\tilde{\omega}_2 + \frac{\omega_p}{2} \right) \frac{\tau}{2} \right] - \phi_L(\gamma_s \tilde{\omega}_1 + \gamma_i \tilde{\omega}_2) \cos \left[\left(\tilde{\omega}_1 + \frac{\omega_p}{2} \right) \frac{\tau}{2} \right] \cos \left[\left(\tilde{\omega}_2 + \frac{\omega_p}{2} \right) \frac{\tau}{2} \right] \right|^2. \quad (\text{A5})$$

Considering again a Gaussian pump spectrum, Eq. (A5) reduces to

$$P_+(\tau) \propto 1 + \cos(\omega_p \tau) \mathcal{F}_1(\tau) + \mathcal{F}_2(\tau), \quad (\text{A6})$$

where

$$\mathcal{F}_1(\tau) \equiv \frac{1}{2} \left\{ e^{-(\Omega_p \tau/2)^2} + \sqrt{\pi} \xi \left[\operatorname{Erf} \left(\frac{1}{4\xi} - \frac{\Omega_p \tau}{2} \right) + \operatorname{Erf} \left(\frac{1}{4\xi} + \frac{\Omega_p \tau}{2} \right) \right] \right\}$$

$$\mathcal{F}_2(\tau) \equiv \frac{1}{2} \left\{ \Lambda(\tau/\tau_\theta) \exp \left[- \left(\frac{\Omega_p \tau}{2} \right)^2 \left(\frac{\cos \theta + \sin \theta}{\cos \theta - \sin \theta} \right)^2 \right] - 2\sqrt{\pi} \xi B(\tau/\tau_\theta) \operatorname{Erf} \left(\frac{1 - |\tau|/\tau_\theta}{4\xi} \right) \right\}, \quad (\text{A7})$$

with $\Lambda(x) = 1 - |x|$ and $B(x) = 1$ for $|x| < 1$, and $\Lambda(x) = B(x) = 0$ elsewhere. The function \mathcal{F}_1 gives an envelope for an oscillation at the pump frequency ω_p , while \mathcal{F}_2 is a contribution that disappears both for the |TB> state and for extended-phase-matched crystals, i.e. in the limit of $\xi \rightarrow \infty$. Notice that in this case Eq. (A6) reduces to Eq. (28). In Fig. 6 some example plots of coincidence graphs are given for different values of the phase-matching parameter θ . As a measure of fringe visibility for the MZ interferometer, we use the quantity

$$V_{MZ} \equiv \frac{P_+(0) - P_+(\pi/\omega_p)}{P_+(0) + P_+(\pi/\omega_p)} = \frac{1 + [\mathcal{F}_1(\pi/\omega_p) - \mathcal{F}_2(\pi/\omega_p)]}{3 - [\mathcal{F}_1(\pi/\omega_p) - \mathcal{F}_2(\pi/\omega_p)]}, \quad (\text{A8})$$

which is plotted as a function of the crystal length L for different values of θ in Fig. 5. In Eq. (A8) the fringe

maximum is estimated by $P_+(0)$, and the fringe minimum is estimated by $P_+(\pi/\omega_p)$; these quantities are easily measured experimentally. Note that for all interesting cases $\mathcal{F}_1(\pi/\omega_p) \geq \mathcal{F}_2(\pi/\omega_p)$, so that Eq. (A8) implies $V_{MZ} \geq 33\%$. This lower bound is reached in the limit of very long crystals $L \rightarrow \infty$ if $\theta \neq -\pi/4$ as shown in Fig. 5. Analogous to the Hong-Ou-Mandel interferometer, the Mach-Zehnder visibility is always maximum for extended phase-matched crystals ($\theta = -\pi/4$).

ACKNOWLEDGMENTS

The Authors thank I. A. Walmsley for making them aware of reference [2]. This work was supported by the DoD Multidisciplinary University Research Initiative (MURI) program administered by the Army Research Office under Grant DAAD 19-00-1-0177 and by the National Reconnaissance Office.

-
- [1] L. Mandel and E. Wolf, *Optical coherence and quantum optics*, Cambridge Univ. press, Cambridge, (1995), Chap. 22.4.
- [2] R. Erdmann, D. Branning, W. Grice, and I. A. Walmsley, *Phys. Rev. A* **62**, 053810 (2000).
- [3] T. E. Keller and M. H. Rubin, *Phys. Rev. A* **56**, 1534 (1997)
- [4] W. P. Grice and I. A. Walmsley, *Phys. Rev. A* **56**, 1627 (1997); W. P. Grice, R. Erdmann, I. A. Walmsley, and

- D. Branning, *Phys. Rev. A*, **57**, R2289 (1998).
- [5] M. Atatüre, A. V. Sergienko, B. M. Jost, B. E. A. Saleh, and M. C. Teich, *Phys. Rev. Lett.* **83**, 1323 (1999); Y.-H. Kim, V. Berardi, M. V. Chekhova, and Y. Shih, *Phys. Rev. A* **64**, 011801(R), (2001); W. P. Grice, A. B. U'Ren, and I. A. Walmsley, *Phys. Rev. A* **64**, 063815 (2001).
- [6] V. Giovannetti, L. Maccone, J. H. Shapiro, and F. N. C. Wong, *Phys. Rev. Lett.* **88**, 183602 (2002).
- [7] M. H. Rubin, D. N. Klyshko, Y. H. Shih, and A. V.

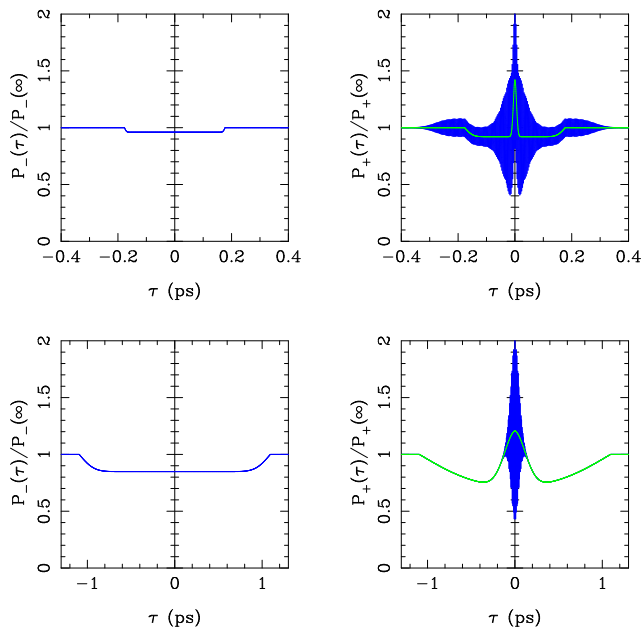


FIG. 6: Plots of the expected coincidence rates for different phase-matching conditions. The two left plots refer to the HOM interferometer setup; the two right plots refer to the MZ interferometer setup. The parameters in the plots are $\theta = \pi/5$ for the two top plots and $\theta = -\pi/6$ for the two bottom plots; $\gamma = 8 \times 10^{-5}$ ps/ μm ; $\omega_p = 2 \times 10^{15}$ s $^{-1}$; $\Omega_p = 4 \times 10^{13}$ s $^{-1}$; $L = 2$ cm. The coincidence rates for the extended phase-matching case ($\theta = -\pi/4$) were plotted in Fig. 4. The degradation of the HOM dip is evident from the left plots. The presence of the function \mathcal{F}_2 in Eq. (A6) is responsible for the fringe modulation in the plots on the right, as compared with the $|\Psi_{epm}\rangle$ case shown in Fig. 4 for which $\mathcal{F}_2 = 0$ prevails.

- Sergienko, Phys. Rev. A **50**, 5122 (1994); J. Perina, Jr., A. V. Sergienko, B. M. Jost, B. E. A. Saleh, and M. C. Teich, Phys. Rev. A **59**, 2359 (1999).
- [8] G. Di Giuseppe, L. Haiberger, F. De Martini, and A. V. Sergienko Phys. Rev. A **56**, R21 (1997); A. V. Sergienko, M. Atatüre, Z. Walton, G. Jaeger, B. E. A. Saleh, and M. C. Teich, Phys. Rev. A **60**, R2622 (1999); D. Branning, W. P. Grice, R. Erdmann, and I. A. Walmsley, Phys. Rev. A **62**, 013814 (2000); Y.-H. Kim, S. P. Kulik, and Y. Shih, Phys. Rev. A **62**, 011802(R) (2000).
- [9] J. H. Shapiro and N. C. Wong, J. Opt. B: Quantum Semiclass. Opt. **2**, L1 (2000).
- [10] J. H. Shapiro in *Proc. of the Seventh International Conf. on Squeezed States and Uncertainty Relations*, Boston, June 2001; C. E. Kuklewicz, E. Keskiner, F. N. C. Wong, and J. H. Shapiro, J. Opt. B: Quantum Semiclass. Opt. **4**, S162 (2002).
- [11] C. K. Hong, Z. Y. Ou, and L. Mandel, Phys. Rev. Lett. **59**, 2044 (1987).
- [12] T. S. Larchuk, R. A. Campos, J. G. Rarity, P. R. Tapster, E. Jakeman, B. E. A. Saleh, and M. C. Teich, Phys. Rev. Lett. **70**, 1603 (1993).
- [13] T. B. Pittman, D. V. Strekalov, A. Migdall, M. H. Rubin, A. V. Sergienko, and Y. H. Shih, Phys. Rev. Lett. **77**, 1917 (1996).
- [14] When type I phase-matched crystals are employed, condition (12) implies $\gamma_s = \gamma_i = 0$. In this case, as already noticed, Eq. (8) is no longer valid and we need to include higher-order contributions [2]. The limits of validity of the first-order Taylor expansion and the generalization of Eq. (12) to higher orders will be discussed at the end of Sect. III.